

Laminar and turbulent groundwater flows in confined two- and three-dimensional discrete fracture networks

Hong Fang^{a,b,*}, Jianting Zhu^b, Jinrong Qiu^a, Yaoming Su^a, Di Xia^a

^a South China Institute of Environmental Sciences, Ministry of Ecology and Environment, Guangzhou 510655, China

^b Department of Civil and Architectural Engineering, University of Wyoming, Laramie, WY 82071, USA

ARTICLE INFO

Keywords:

Groundwater flowrate
Laminar flow
Turbulent flow
Fracture network
Reynolds number

ABSTRACT

Using laminar or turbulent flow equations indiscriminately to describe groundwater flows in fracture networks may result in large errors. We propose a new method for simulating steady-state groundwater flows in two- and three-dimensional fracture networks by separating laminar flows and turbulent flows in individual fractures. Poiseuille's law is employed when the flow is laminar, while Swamee and Jain formula is utilized when the flow is turbulent. The model results are first compared to recently measured field groundwater flow data in a mining tunnel network. The effect of hydraulic gradient, aperture, fracture width in the third dimension, and fracture density is then examined. Using the laminar flow equation indiscriminately in all fractures overestimates groundwater flowrates, whereas using the turbulent flow equation underestimates them. The aperture contrast of large and small fractures has a significant impact on the potential errors of indiscriminately applying the laminar or turbulent flow equation and the flowrate difference between the three-dimensional and two-dimensional fracture networks. Total groundwater flowrates increase with fracture density in both three-dimensional and two-dimensional fracture networks, with the largest increase occurring when additional fractures are introduced parallel to the hydraulic gradient. The new approach may be utilized to estimate hydraulic head distribution and groundwater flowrate according to the crack patterns and geometric properties of the fractured rock.

1. Introduction

Groundwater flow in fractured rock networks is critically important in many applications such as water resource management (Pan et al., 2010; Ren et al., 2015), contaminant transport (Brutz and Rajaram, 2017; Klammler et al., 2016), nuclear waste migration, hydrocarbon exploitation (Follin and Stigsson, 2014; Mattila and Tammisto, 2012) and tunneling in aquifers (Lee and Moon, 2004; Butscher et al., 2011; Mathurin et al., 2012). There have been numerous studies on groundwater flows in fracture networks in recent years (Chesnaux et al., 2009; Ji and Koh, 2017; Huang et al., 2019). Two of the most common approaches for modeling groundwater flow across fractured rock are continuum and discrete fracture network (DFN) models. Continuum models are built on the concept of representative elementary volume (REV), in which the fractured domain is homogenized as an equivalent continuum at an appropriate scale (Agharazi et al., 2015; Gan and Elsworth, 2016; Hadgu et al., 2017; Oliver et al., 2015). However, determining equivalent hydrological properties, such as hydraulic conductivity, is challenging since the equivalent continuum is difficult

to be properly defined, especially for sparse fractures (Tang et al., 1998; Adler and Thovert, 1999; Guo et al., 2017). In most fractured rocks, groundwater is mainly transported by highly permeable fractures, and the flow in the matrices is negligible (Carrier and Granet, 2012; Huang et al., 2017). In these cases, the DFN approach has the advantage of explicitly representing the geometrical properties of the network such as location, size, orientation, and aperture of any individual fracture in the network (Dippenaar and Van Rooy, 2016; Aldrich et al., 2017; Karimzade et al., 2017; Huang et al., 2020).

The significant computational demand involved with the detailed depiction of the fracture network is one of the limitations of DFN models and it increases considerably as the number of fractures, network density, and length scales increase. Due to the computational constrain, the DFN model either depicted the network as a collection of connected pipes (Dershowitz, 1999; Jing et al., 2020; Xu and Hu, 2017) or used two-dimensional representations (Li et al., 2020). In this study, a graph-based technique is used for groundwater flows through sparse fracture networks. The core of the technique is the construction of a graph representation of a DFN based on its topology and fracture properties. In

* Corresponding author at: South China Institute of Environmental Sciences, Ministry of Ecology and Environment, Guangzhou 510655, China.
E-mail address: fanghong@scies.org (H. Fang).

sparse fracture networks, the dominating flow is highly influenced by network topology (Gong and Rossen, 2016) and the imposed flow direction (Jourde et al., 2002). As a result, the network's representation can capture the key characteristics that determine where flow channeling occurs and identify the primary flow pathways with the fewest prominent fractures between the inlet and outlet. In two-dimensional discrete fracture network models, the third dimension of fracture is assumed to be infinite (Cliffe et al., 2011; Parashar and Reeves, 2012; Reeves et al., 2013). While the two-dimensional fractures are convenient, the groundwater flow predictions may be overestimated or underestimated (Karimzade et al., 2017).

The three-dimensional discrete fracture network models in the past typically treated groundwater flow behaviors indiscriminately in all individual fractures by assuming either laminar or turbulent flow (Hyman et al., 2017; Wu et al., 2012). Fracture rock networks in nature, however, often have a diverse range of fracture properties such as aperture size, density, orientation, and length. Therefore, laminar and turbulent flows may coexist in different fractures of the fractured rocks. When the flow is laminar, the turbulent flow equation underestimates the actual flowrate, whereas the laminar flow equation considerably overestimates the flowrate when the flow is turbulent. As a result, indiscriminately using either the laminar or turbulent flow equation in all fractures may introduce large errors.

In this study, we propose a new and improved approach for simulating steady-state groundwater flow behavior in a fracture network where both laminar and turbulent flows may coexist in different parts of the network, as shown in Fig. 1a. The Poiseuille's law (Sutera and

Skalak, 1993) is applied when the flow is laminar while the Swamee and Jain formula (Swamee and Jain, 1976) is applied when the flow is turbulent in a fracture. The flow equations are iteratively solved until the solutions satisfy the groundwater flow equations in all the fractures. The Reynolds number (Re) in each fracture is explicitly determined at each iteration step and used to judge whether the groundwater flow in that fracture is laminar or turbulent. The focus of this study is two-fold. The first focus is to examine the potential errors in groundwater flowrates caused by indiscriminately applying the laminar flow equation or the turbulent flow equation to all fractures without specifically accounting for the actual groundwater flow characteristics in particular fractures. The second one is to investigate the difference between groundwater flows predicted by three-dimensional discrete fracture network models and those predicted by two-dimensional discrete fracture network models. The new approach is first compared against field measurements of groundwater flowrate from the Lead-zinc Mining Area in Guangdong province, China. The main point of discussion in the two aspects is then the influence of the overall hydraulic gradient, the aperture, the width of fractures in the third dimension, and the fracture density. This conceptualization can be applied in any natural fracture networks where rock volumes are often intersected by a few dominant fractures. Based on the crack patterns and the geometric characteristics of the fractured rock, this improved approach can be used to estimate the hydraulic head distribution and predict the groundwater flowrate.

2. Methodology

2.1. Model formulation

While the method can be applied to any fracture network configuration, we employ a simple fracture network, as illustrated in Fig. 1b, to demonstrate the main ideas of the proposed approach. A higher hydraulic head is applied on the left-hand side of the domain, and therefore, the overall groundwater flow direction is from left to right. Additionally, the rock matrix in the fracture network is assumed to be impermeable, as discussed earlier. It is also assumed that the minor head loss at the nodes can be neglected compared to the major loss due to friction in the fractures. The simple fracture network in Fig. 1b is made up of 27 nodes and 54 fractures. To characterize the flow behaviors in each fracture, flow equations based on the hydraulic head difference are utilized. The hydraulic heads at the inlets (Nodes 1, 4, 7, 10, 13, 16, 19, 22, and 25) and the outlets (Nodes 3, 6, 9, 12, 15, 18, 21, 24, and 27) are given as the boundary conditions. The hydraulic heads at the internal nodes $h_2, h_5, h_8, h_{11}, h_{14}, h_{17}, h_{20}, h_{23},$ and h_{26} and the flowrate at the inlets $Q_1, Q_4, Q_7, Q_{10}, Q_{13}, Q_{16}, Q_{19}, Q_{22}, Q_{25}$ as well as the flowrate at the outlets $Q_3, Q_6, Q_9, Q_{12}, Q_{15}, Q_{18}, Q_{21}, Q_{24},$ and Q_{27} need to be solved iteratively for a total of 27 unknowns. We can construct 27 groundwater flow equations based on the mass conservation requirement at the 27 internal nodes for the 27 unknown variables. The groundwater flow equations can be linear, non-linear, or a mixture of both in terms of the unknown hydraulic heads at each iteration step, depending on the groundwater flow behaviors in any specific fractures. The Newton-Raphson iteration approach is used to iteratively solve for the unknown flowrates and hydraulic heads because the groundwater flow behaviors are unknown beforehand.

Note that the groundwater flow directions in all the fractures are also unknown, which need to be solved iteratively. For example, the conservation requirement at Node 14 along with the assumed groundwater flow directions in the fractures connected to Node 14 leads to the following equation,

$$Q_{5-14} + Q_{13-14} + Q_{11-14} - Q_{14-15} - Q_{14-17} - Q_{14-23} = 0 \quad (1)$$

where the positive sign represents the groundwater flow toward Node 14 while the negative sign denotes the groundwater flow away from Node 14. The actual flow direction in each fracture is determined at each

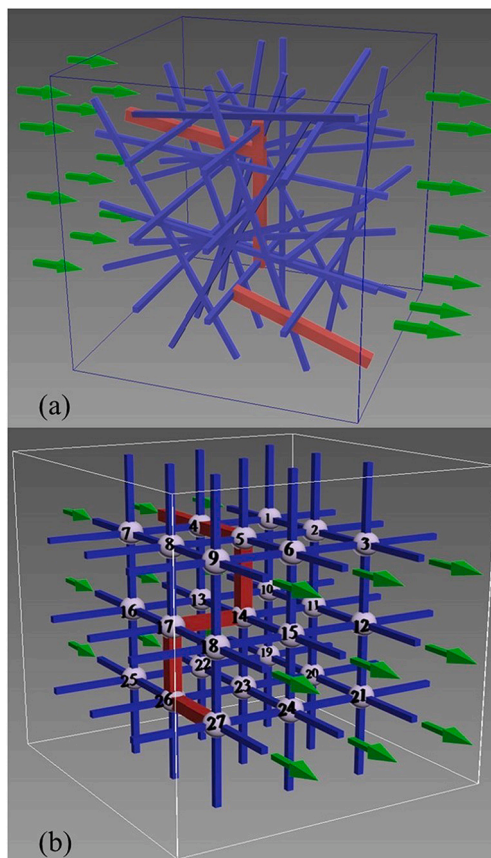


Fig. 1. (a) A three-dimensional irregular fracture network domain where laminar and turbulent flow may exist simultaneously, and (b) schematic view of groundwater flow through a regular fracture network. The blue and red color denotes the small and large fractures, individually. (For interpretation of the references to color in this figure legend, the reader is referred to the web version of this article.)

iterative step as part of the solution process.

If flow in a fracture is laminar, the Poiseuille's law (Sutera and Skalak, 1993) is used,

$$Q = \frac{\rho g \pi D_{i-j}^4}{128 \mu} \cdot \frac{(h_i - h_j)}{\Delta L_{i-j}} \quad (2)$$

where ρ is the density of water, g is the gravitational acceleration, μ is the dynamic viscosity of water, h_i is the hydraulic head at Node i , D_{i-j} is the hydraulic diameter of the fracture between Nodes i and j , and ΔL_{i-j} is the fracture length between Nodes i and j . If the cross-section is rectangular, the hydraulic diameter is equal to $2ab/(a + b)$ where a and b denote the width and aperture, respectively.

If all the flows in the fractures connecting to Node 14 are laminar, Eq. (1) for Node 14 can be expressed as,

$$\begin{aligned} & \frac{\rho g \pi D_{5-14}^4}{128 \mu} \cdot \frac{(h_5 - h_{14})}{\Delta L_{5-14}} + \frac{\rho g \pi D_{13-14}^4}{128 \mu} \cdot \frac{(h_{13} - h_{14})}{\Delta L_{13-14}} + \frac{\rho g \pi D_{11-14}^4}{128 \mu} \\ & \cdot \frac{(h_{11} - h_{14})}{\Delta L_{11-14}} - \frac{\rho g \pi D_{14-15}^4}{128 \mu} \\ & \frac{(h_{14} - h_{15})}{\Delta L_{14-15}} - \frac{\rho g \pi D_{14-17}^4}{128 \mu} \cdot \frac{(h_{14} - h_{17})}{\Delta L_{14-17}} - \frac{\rho g \pi D_{14-23}^4}{128 \mu} \cdot \frac{(h_{14} - h_{23})}{\Delta L_{14-23}} = 0 \end{aligned} \quad (3)$$

If flow in a fracture is turbulent, the equation by Swamee and Jain (1976) is used to determine flowrate Q in each fracture,

$$Q = -0.965 \left(\frac{g D_{i-j}^5 (h_i - h_j)}{\Delta L_{i-j}} \right)^{0.5} \ln \left[\frac{\varepsilon}{3.7 D_{i-j}} + \left(\frac{3.17 \Delta L_{i-j}}{g D_{i-j}^3 (h_i - h_j)} \cdot \frac{\mu^2}{\rho^2} \right) \right] \quad (4)$$

where ε is the roughness, which may vary from 0 to close to 1 m for very rough rock surface of large tunnels (Montecinos and Wallace, 2010). In this study, we use a relatively large roughness of 0.013 m (Montecinos and Wallace, 2010). It should be noted, however, that any roughness values can be incorporated into the developed method in this study.

If all the flows in the fractures connecting Node 14 are turbulent, Eq. (1) for Node 14 can be expressed as,

$$\begin{aligned} & 0.965 \left(\frac{g D_{5-14}^5 (h_5 - h_{14})}{\Delta L_{5-14}} \right)^{0.5} \ln \left[\frac{\varepsilon}{3.7 D_{5-14}} + \left(\frac{3.17 \Delta L_{5-14}}{g D_{5-14}^3 (h_5 - h_{14})} \cdot \frac{\mu^2}{\rho^2} \right) \right] \\ & + 0.965 \left(\frac{g D_{13-14}^5 (h_{13} - h_{14})}{\Delta L_{13-14}} \right)^{0.5} \ln \left[\frac{\varepsilon}{3.7 D_{13-14}} + \left(\frac{3.17 \Delta L_{13-14}}{g D_{13-14}^3 (h_{13} - h_{14})} \cdot \frac{\mu^2}{\rho^2} \right) \right] \\ & + 0.965 \left(\frac{g D_{11-14}^5 (h_{11} - h_{14})}{\Delta L_{11-14}} \right)^{0.5} \ln \left[\frac{\varepsilon}{3.7 D_{11-14}} + \left(\frac{3.17 \Delta L_{11-14}}{g D_{11-14}^3 (h_{11} - h_{14})} \cdot \frac{\mu^2}{\rho^2} \right) \right] \\ & - 0.965 \left(\frac{g D_{14-15}^5 (h_{14} - h_{15})}{\Delta L_{14-15}} \right)^{0.5} \ln \left[\frac{\varepsilon}{3.7 D_{14-15}} + \left(\frac{3.17 \Delta L_{14-15}}{g D_{14-15}^3 (h_{14} - h_{15})} \cdot \frac{\mu^2}{\rho^2} \right) \right] \\ & - 0.965 \left(\frac{g D_{14-17}^5 (h_{14} - h_{17})}{\Delta L_{14-17}} \right)^{0.5} \ln \left[\frac{\varepsilon}{3.7 D_{14-17}} + \left(\frac{3.17 \Delta L_{14-17}}{g D_{14-17}^3 (h_{14} - h_{17})} \cdot \frac{\mu^2}{\rho^2} \right) \right] \\ & - 0.965 \left(\frac{g D_{14-23}^5 (h_{14} - h_{23})}{\Delta L_{14-23}} \right)^{0.5} \ln \left[\frac{\varepsilon}{3.7 D_{14-23}} + \left(\frac{3.17 \Delta L_{14-23}}{g D_{14-23}^3 (h_{14} - h_{23})} \cdot \frac{\mu^2}{\rho^2} \right) \right] \\ & = 0 \end{aligned} \quad (5)$$

Accordingly, similar groundwater flow equations can be developed for other nodes in the fracture network.

As an initial guess, we may use Eq. (3) to solve for all the unknown flowrates and the hydraulic heads. From the results in the first iteration, the Re value is obtained and the flow behavior (laminar or turbulent) is

determined in every fracture. For instance, if the groundwater flows in the fractures from Node 5 to Node 14, and Node 14 to Node 17 are turbulent, and the flows are laminar in the other fractures, we need to use the following equation for the next step of the iteration,

$$\begin{aligned} & 0.965 \left(\frac{g D_{5-14}^5 (h_5 - h_{14})}{\Delta L_{5-14}} \right)^{0.5} \ln \left[\frac{\varepsilon}{3.7 D_{5-14}} + \left(\frac{3.17 \Delta L_{5-14}}{g D_{5-14}^3 (h_5 - h_{14})} \cdot \frac{\mu^2}{\rho^2} \right) \right] \\ & + \frac{\rho g \pi D_{13-14}^4}{128 \mu} \cdot \frac{(h_{13} - h_{14})}{\Delta L_{13-14}} + \frac{\rho g \pi D_{11-14}^4}{128 \mu} \cdot \frac{(h_{11} - h_{14})}{\Delta L_{11-14}} \\ & - \frac{\rho g \pi D_{14-15}^4}{128 \mu} \cdot \frac{(h_{14} - h_{15})}{\Delta L_{14-15}} - \frac{\rho g \pi D_{14-23}^4}{128 \mu} \cdot \frac{(h_{14} - h_{23})}{\Delta L_{14-23}} \\ & - 0.965 \left(\frac{g D_{14-17}^5 (h_{14} - h_{17})}{\Delta L_{14-17}} \right)^{0.5} \ln \left[\frac{\varepsilon}{3.7 D_{14-17}} + \left(\frac{3.17 \Delta L_{14-17}}{g D_{14-17}^3 (h_{14} - h_{17})} \cdot \frac{\mu^2}{\rho^2} \right) \right] \\ & = 0 \end{aligned} \quad (6)$$

Similar equations for all other internal nodes can be developed accordingly. We also use the Newton-Raphson method to solve these non-linear equations. While the iteration process is started from laminar flow Eq. (3) in this study, it should be emphasized that starting from laminar flow or turbulent flow has no effect on the final solutions. The convergent solution can be reached faster, however, when the iteration is started from the laminar equation. Although Eq. (5) is nonlinear, the proposed model represents a physically meaningful problem and has a unique solution.

After solving for the groundwater flowrates in all the fractures and the hydraulic heads at all the nodes, we can analyze the groundwater flow in each fracture and overall groundwater flowrate. As discussed earlier, we primarily discuss the potential errors in the groundwater flowrate in the three-dimensional fracture network caused by indiscriminately assuming uniform flow behavior (i.e., either laminar or turbulent) in all individual fractures, as well as the differences between the three-dimensional and two-dimensional flow scenarios. In doing so, we define two errors in percentage as follows in Eqs. (7) and (8).

$$E_r = \frac{Q_u - Q}{Q} \cdot 100\% \quad (7)$$

where Q_u denotes the flowrate determined by using the uniform flow behavior in all fractures (i.e., either the Poiseuille's law or the Swamee and Jain formula), Q is the flowrate calculated by the proposed new approach of explicitly distinguishing turbulent and laminar flows.

$$D_r = \frac{Q_{3D} - Q_{2D}}{Q_{3D}} \cdot 100\% \quad (8)$$

where Q_{2D} denotes the flowrate obtained from the two-dimensional network model, and Q_{3D} is the flowrate calculated by the three-dimensional network model.

2.2. Model comparison with measured groundwater flow data

Recently measured field groundwater flow data at the Lead-zinc Mining Area located in Guangdong province, China (Fig. 2a) are used to validate the model. This field site has an undulating low mountain and hilly landform, with high terrain in the south and east and low terrain in the north and west with a natural slope of 25–35°. Three inclined shafts have been opened at the mine site. The underground mining range is approximately 400 m long from east to west and 200 m wide from north to south with the linked mining channels as shown in Fig. 2b. In and around the mining region, there is no considerable surface water distribution. During the dry season, the water supply is mostly sourced from the mountains to the south and east of the mining region and delivered through fractures in the contact zone between the granite

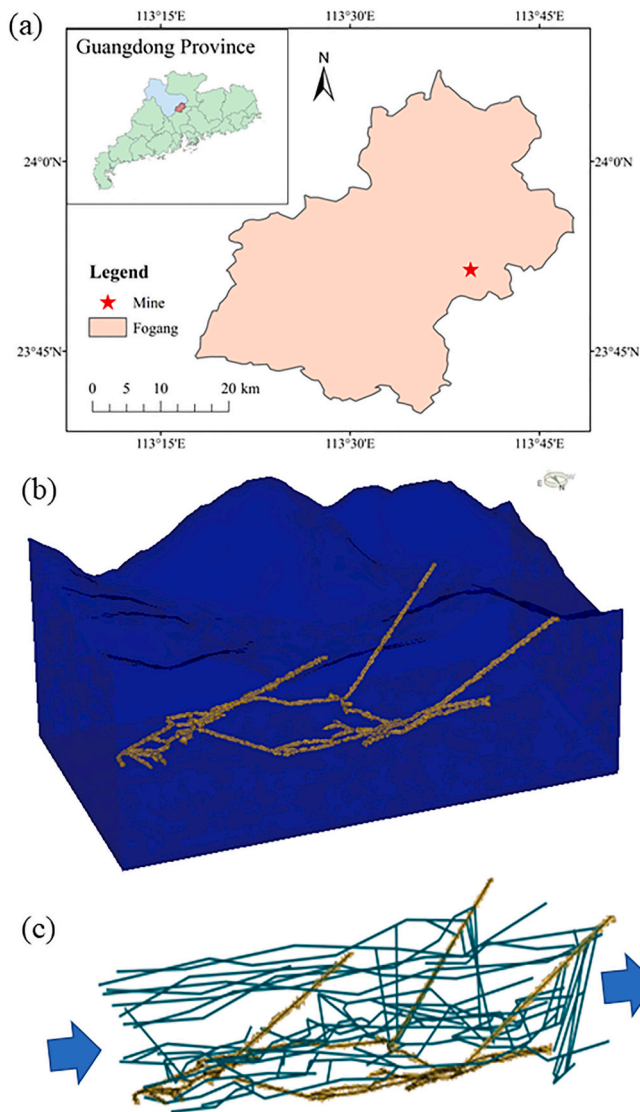


Fig. 2. Location of the lead-zinc mining area in Guangdong province in southern China (a) and distribution of the mine tunnels (b) and (c). The gold lines in (c) indicate the large fractures, the green lines in (c) indicate the small fractures and the blue arrows in (c) indicate the main flow direction. (For interpretation of the references to color in this figure legend, the reader is referred to the web version of this article.)

ceiling and strata. Massive rock fracture aquifers and stratified rock fracture aquifers are the two basic types of aquifers in the region. The underground tunnel links to the aquifer and serves as a connecting channel between the aquifers, accelerating groundwater flow and discharge via the underground tunnel.

The flow measurements were taken starting from the middle of March 2022, during the dry season with no rain in two months such that flow was mainly at steady state. The depth to the groundwater was 11.16–11.80 m. Nineteen observation wells were set up to monitor the hydraulic head and flow gauges were used to measure the total flowrate through the mine tunnel. The small fractures are treated as tubes with hydraulic diameters from 0.005 m to 0.02 m and the mine tunnels are considered as tubes with hydraulic diameters from 1 m to 1.5 m according to the hydrogeological survey and drawings provided by the mine owner.

In Fig. 2c, the hydraulic head of the high terrain is set as 165 m, while the hydraulic head of the low terrain is set as 150 m based on the field measured values. A critical Reynolds number of 2300 (Sarpkaya, 1966)

is used to determine the flow regimes and can automatically identify the groundwater flow in the tunnel as turbulent flow, and that in the small fractures as laminar flow.

3. Results

Fig. 3 shows a comparison of measured flowrate data and simulated results from March 15 to April 30 using the three approaches. The measured flowrate in Fig. 3 is the total of all the fracture flowrates, including those from the mine tunnels and the small fractures. During this period, there was no significant variation in the total flowrate, which means the flow was approximately at steady state. Using Poiseuille's law indiscriminately predicts the highest flowrates among the three approaches, which greatly over-estimates the observed flowrate. Using the Swamee and Jain formula indiscriminately yields the lowest values, which under-estimates the observed flowrate. The new approach in this study produces the results closest to the measured flowrate. The mine tunnels carry the majority of the flowrate and act as the principal flow conduit. Assuming the flow is laminar when it is actually turbulent in the mine tunnel leads to large errors. On the other hand, treating the flow as turbulent when it is actually laminar causes inaccuracy in small fractures, but the overall error is significantly lower than assuming the flow is laminar in all the mine tunnels. The comparison results demonstrate that explicitly distinguishing turbulent flow and laminar flow and solving them separately can greatly improve the accuracy of flowrate prediction. However, mainly due to the tortuosity of the mine tunnel, the flowrate results of the new approach are still somewhat greater than the observed data.

In the remainder of this section, we present and discuss simulation results using a few relatively simple fracture network configurations to examine how flows in the third dimension affect total groundwater flows and how the potential errors in flowrate calculations caused by not separately considering flow behaviors in different fractures are related to the overall hydraulic gradient, aperture of fractures, width in the third dimension, and network density of fractures. Although we can only present and discuss the results for a few fracture networks, the approach is applicable to any configuration of three-dimensional fracture network. In calculating the quantitative results, several input parameters are required including $g = 9.8 \text{ m/s}^2$, $\rho = 1000 \text{ kg/m}^3$, $\mu = 0.0011 \text{ kg/(m s)}$ and the critical Reynolds number of 2300 (Sarpkaya, 1966) to distinguish laminar flow and turbulent flow in each fracture.

In the first case, the groundwater flow behaviors for the two fracture networks depicted in Fig. 4 are simulated using the previously mentioned approaches. Fig. 4a depicts a two-dimensional fracture network, whereas Fig. 4b depicts a three-dimensional fracture network. The fractures are distributed in a rectangle domain with 1000 nodes (i.e., $10 \times 10 \times 10$) in the three-dimensional configuration shown in Fig. 4b. The apertures of the small (in light color) and the large fractures (in dark color) are 0.005 m and 0.025 m for both networks, respectively. Both fracture networks have a total domain height of 9 m. To be comparable between these two fracture network configurations, the sum of

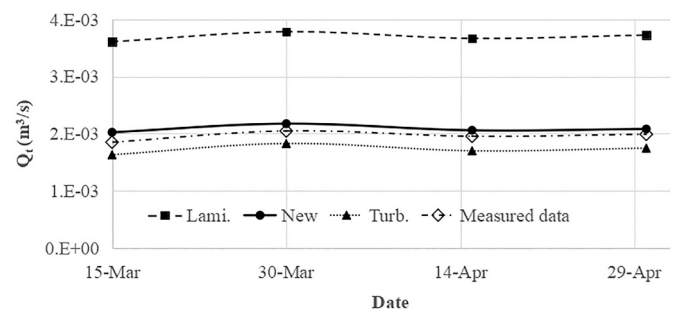


Fig. 3. Comparison of the total flowrate between the simulated results and the measured data.

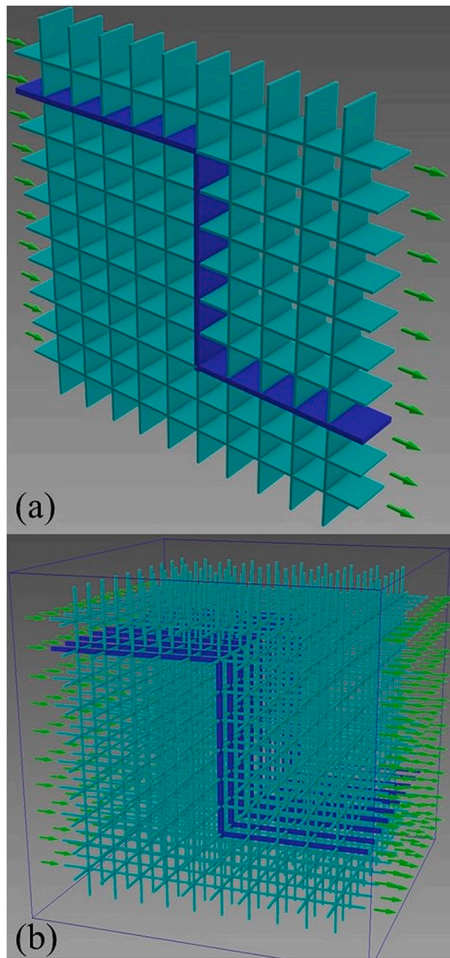


Fig. 4. The example configurations of the fracture networks to illustrate groundwater flowrate results, (a) two-dimensional fracture network, and (b) three-dimensional fracture network. Dark color indicates large fractures and light color indicates small fractures.

the widths of the fractures in the third dimension at the same elevation in the three-dimensional network should be equal to the width of the fracture in the two-dimensional network. The widths of the large fractures in the vertical direction, seen in dark color in the third dimension, vary in the three-dimensional fracture network in Fig. 4b. For the five large fractures in the vertical direction near the front side, the width is set to be 0.06 m while that for the five large vertical fractures near the back side is 0.04 m. Then for the two-dimensional network in Fig. 4a, the width for the large fracture would be 0.5 m, which is equal to the total width of all 10 large fractures in the third dimension. Although the total cross-sectional area of the fractures in the three-dimensional fracture network is the same as that in the two-dimensional network, the contrast of the fracture width would lead to the groundwater flow in the third dimension and the differences in the flow behaviors between the three-dimensional and two-dimensional fracture networks.

The simulations for both the three-dimensional and two-dimensional fracture networks are performed with the imposed overall hydraulic head difference of 1 m between the left-hand and the right-hand sides. The total length of the fracture network domain varies from 10,000 m to 167 m, which leads to the overall hydraulic gradients in the range from 0.0001 to 0.006. The results of the total flowrate Q , flowrate of the single large fracture in three-dimensional network, flowrate of the single large fracture in two-dimensional network, the percent flowrate error E_r of indiscriminately applying the Poiseuille's law or the Swamee and Jain formula for all fractures, and the percent difference of total flowrate D_r

between the three-dimensional and two-dimensional fracture networks are plotted as a function of the overall hydraulic gradient in Fig. 5a. Flows in all fractures are laminar and the flowrate results from the new approach are identical to those from the Poiseuille's law when the overall hydraulic gradient is low. While the flows in the small fractures remain laminar when the overall hydraulic gradient increases, the flows in the large fractures may become turbulent. Because the Poiseuille's law overestimates the flowrate in large fractures, especially in the two-dimensional fracture networks, the flowrate through the networks from only applying the Poiseuille's law for all fractures becomes larger than that from the new approach. On the other hand, the Swamee and Jain formula without explicitly considering flow regimes under-estimates the flowrate through these two networks because the frictional loss is over-estimated when the flow is laminar in some fractures.

The flowrate and hydraulic gradient relations in a single large fracture is depicted in Fig. 5b and c. The flowrate in the single large fracture, similar the total flowrate, quickly increases in a non-linear manner as the hydraulic gradient increases. When the hydraulic gradient increases and the flows become turbulent, the flowrate calculated by the new approach is lower than the Poiseuille's law but higher than the Swamee and Jain formula. Because there are also flows in the third dimension, a clear distinction exists between the new approach and the Swamee and Jain formula. From Fig. 5d we can observe that the percent error from indiscriminately applying the Poiseuille's law increases faster in the two-dimensional network than in the three-dimensional network as the overall hydraulic gradient increases. This is due to the greater over-estimation of flowrates in the large fractures in the two-dimensional network, which dominates the total flowrate in the fracture network. The percent errors also increase from only applying the Swamee and Jain formula due to its under-estimation of flowrates in the small fractures.

Fig. 5e shows that the flowrate results from the three-dimensional and two-dimensional fracture networks differ for all three approaches described previously, even though the total fracture areas at the inlet and outlet are the same for both networks. Under the same conditions, the overall groundwater flowrate in the three-dimensional fracture network is greater than that in the two-dimensional network. The relative difference between the three-dimensional and two-dimensional fracture networks remains constant as the hydraulic gradient varies applying the Poiseuille's law since the flowrate is linearly proportional to the hydraulic gradient. The existence of fractures in the third dimension for the three-dimensional fracture network can facilitate flows to minimize frictional energy loss. As a result, the total flowrate in the three-dimensional fracture network is higher than that in the two-dimensional counterpart.

In the second case, we examine the impact of aperture of large fractures on the groundwater flowrate for the fracture network configurations shown in Fig. 4. The aperture of the small fractures is 0.005 m in these two fracture network domains in Fig. 4a and b. The applied overall hydraulic gradient is 0.006 for both the two-dimensional and three-dimensional fracture networks. The aperture of large fractures in both fracture networks varies from 0.01 m to 0.05 m. Fig. 6 shows the influence of aperture of large fractures on the total flowrate (Fig. 6a), the percent flowrate error E_r from the Poiseuille's law and the Swamee and Jain formula (Fig. 6b), and the flowrate difference D_r between the three-dimensional and two-dimensional fracture networks (Fig. 6c). As expected, the total flowrate increases significantly with the aperture of large fractures since these large fractures are mainly responsible for the groundwater flowrate. The percent error from applying the Poiseuille's law indiscriminately increases dramatically when the aperture of large fractures in the two-dimensional fracture network grows (Fig. 6b). Conversely, applying the Swamee and Jain formula indiscriminately in all fractures results in an under-estimation of flowrates in small fractures, as evidenced by the negative percent errors in Fig. 6b. The increase in the aperture of large fractures results in turbulent flows in a high proportion of the fractures. Therefore, the underestimation errors

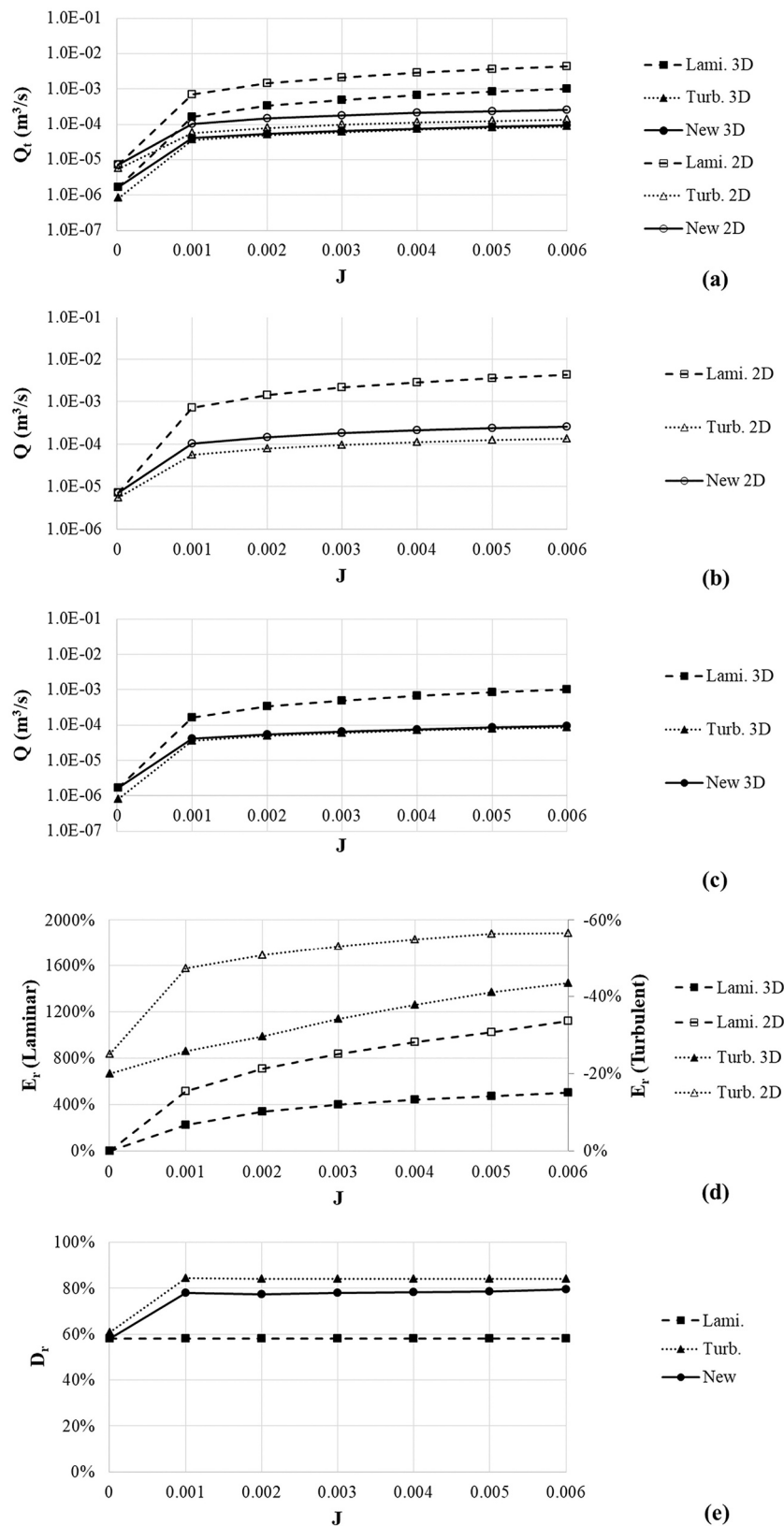


Fig. 5. Flowrate results as a function of the imposed overall hydraulic gradient for the three-dimensional and the two-dimensional network in Fig. 4, (a) total flowrate, (b) flowrate of the single large fracture in three-dimensional network, (c) flowrate of the single large fracture in two-dimensional network, (d) percent flowrate errors, and (e) flowrate difference between the three-dimensional network and the two-dimensional network.

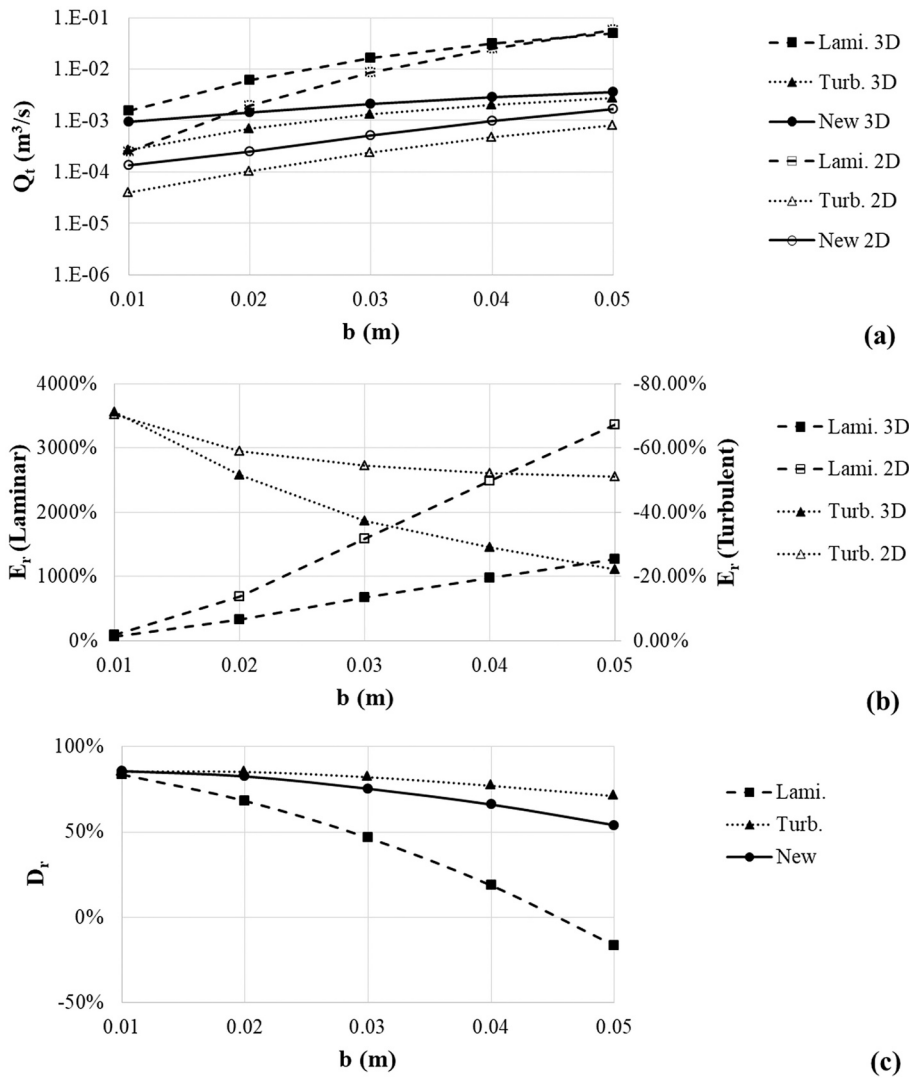


Fig. 6. Flowrate results as a function of the aperture of large fractures for the network in Fig. 4, (a) flowrate, (b) percent flowrate errors, and (c) flowrate difference between the three-dimensional network and the two-dimensional network.

of indiscriminately using the Swamee and Jain formula decrease with the aperture of large fractures. Since the Swamee and Jain formula under-estimates the flowrate when the flows are laminar, the percent error is mainly produced in the small fractures where the flows are laminar.

From Fig. 6c, it can be noted that the differences of groundwater flowrates between the three-dimensional and two-dimensional fracture networks from all three approaches decrease with increasing aperture of the large fractures. As the aperture increases, the groundwater flow in the network is increasingly turbulent and the significance of flow in the third direction diminishes, which reduces the difference of flowrates in the three-dimensional and two-dimensional fracture networks.

The influence of overall width in the third dimension on groundwater flow behaviors is examined in the third case of the fracture configurations in Fig. 4 by varying the total width of the three-dimensional network in the third dimension from 9 m to 100 m. The total width of the fractures, however, remains the same to be 0.5 m for both the three-dimensional and two-dimensional networks. Therefore, the lengths of connecting fractures in the third dimension for the three-dimensional fracture network increase as the total width increases. Because the total width in the two-dimensional fracture network is the same, the total flowrates in the two-dimensional fracture network do not change.

Fig. 7 shows the influence of the width of the three-dimensional

network on the total flowrate Q_t (Fig. 7a), the percent error E_r (Fig. 7b), and the flowrate difference D_r between the three-dimensional and two-dimensional networks (Fig. 7c). Due to the reason described earlier, the total flowrate in the two-dimensional fracture network does not change with the total width. While the fractures in the third dimension can facilitate overall groundwater flows as they allow self-regulation, the frictional loss also proportionally increases as the lengths of these connecting fractures in the third-dimension increase. These two competing mechanisms explain the total groundwater flowrate decrease with increasing total width in the third dimension for the three-dimensional fracture network (Fig. 7a). However, the extent of the decrease is determined by the approach used, with the percent errors decreasing most with the total width by applying the Poiseuille's law. As the lengths of the small connecting fractures in the third-dimension increase, the overall groundwater behaviors become more likely to be laminar, which explains the decrease in the percent errors from indiscriminately using the Poiseuille's law as the total width increases. On the other hand, the same reason can be used to explain the increase of the percent errors by indiscriminately using the Swamee and Jain formula (Fig. 7b). For the two-dimensional network, the total flowrates and the relative errors do not change with the total width in the third dimension.

As shown in Fig. 7c, as the total width of three-dimensional fracture

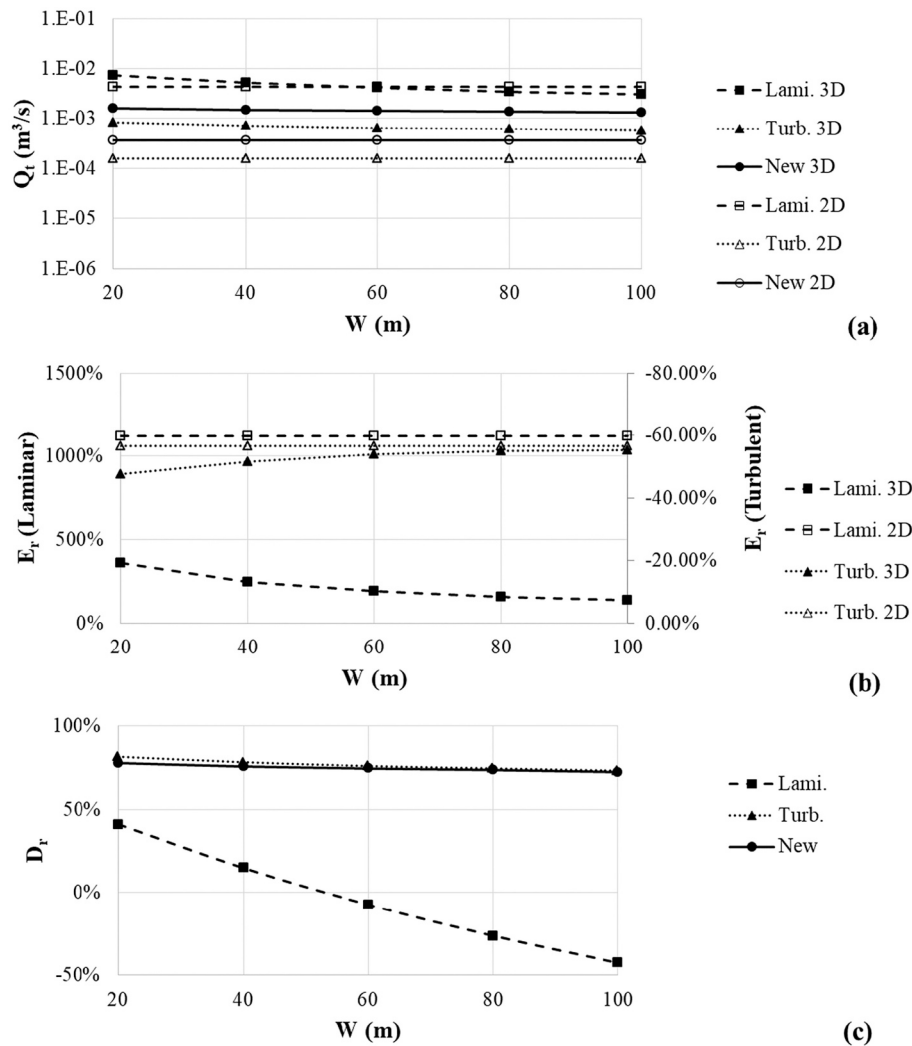


Fig. 7. Flowrate results as a function of the width in the third dimension for the network in Fig. 4, (a) flowrate, (b) percent flowrate errors, and (c) flowrate difference between the three-dimensional network and the two-dimensional network.

network increases, the difference in the total flowrate between the three-dimensional and two-dimensional fracture networks decreases, indicating that the flowrate in the three-dimensional network decreases as the total width increases. One noticeable trend seen from Fig. 7c is that the difference between the three-dimensional and two-dimensional fracture networks decreases by the largest extent from applying the Poiseuille’s law. The proposed approach more precisely reflects the actual flow characteristics in the fractures by appropriately distinguishing turbulent flows and laminar flows in all fractures. It should be noted, however, that while Poiseuille’s law predicts the greatest flowrate decline owing to an increase in fracture network width, the actual flowrate predicted by Poiseuille’s law is still significantly larger than the other two approaches (Fig. 7a).

In the fourth case, all the approaches are used to simulate fracture networks with variable relative fracture density. The fracture density in the two-dimensional fracture network in Fig. 8 is increased by adding more diagonal small fractures to the network in Fig. 4a, whereas more diagonal small fractures are added to the three-dimensional regular network in Fig. 4b, as shown in Fig. 9. Fig. 9 only exhibits a portion of the three-dimensional networks. The entire fracture network domain is the same as that shown in Fig. 4. The apertures of small and large fractures are 0.005 m and 0.025 m, respectively, and the overall hydraulic gradient of 0.006 is applied to all networks. The relative density of the most dense networks shown in Fig. 8d and Fig. 9d is defined as 1

for the two-dimensional and three-dimensional networks, respectively. The two-dimensional fracture network has the maximum number of fractures with 261. The relative densities of the two-dimensional fracture networks in Fig. 4a and Figs. 8a – 8d are 0.69, 0.77, 0.79, 0.85 and 1, respectively. The three-dimensional fracture network has the maximum number of fractures with 5589. The relative density of the fracture network in Fig. 4b is therefore equal to $2430/5589 = 0.43$. The other relative densities of the three-dimensional networks in Figs. 9a – 9d are 0.58, 0.72, 0.87 and 1, respectively.

Fig. 10 plots the simulation results in both the three-dimensional and two-dimensional fracture networks at various relative densities, which show the total flowrates in the fracture network increase as the density of fractures increases. Since the overall domain size and overall hydraulic gradient are the same, more fractures in the network simply mean more groundwater flows can occur, which results in the increasing flowrates. Because additional diagonal fractures have the small aperture, larger density means more small fractures which results in a larger portion of the laminar flows in fracture networks. Therefore, the percent errors from using the Poiseuille’s law decrease as the density increases for both the three-dimensional and two-dimensional fracture networks, as shown in Fig. 10b. Note that in Fig. 10a, the three-dimensional network density increases from 0.58 to 0.72 which is a result of adding more fractures in the faces perpendicular to the hydraulic gradient. The small increase in flowrate when the three-dimensional network

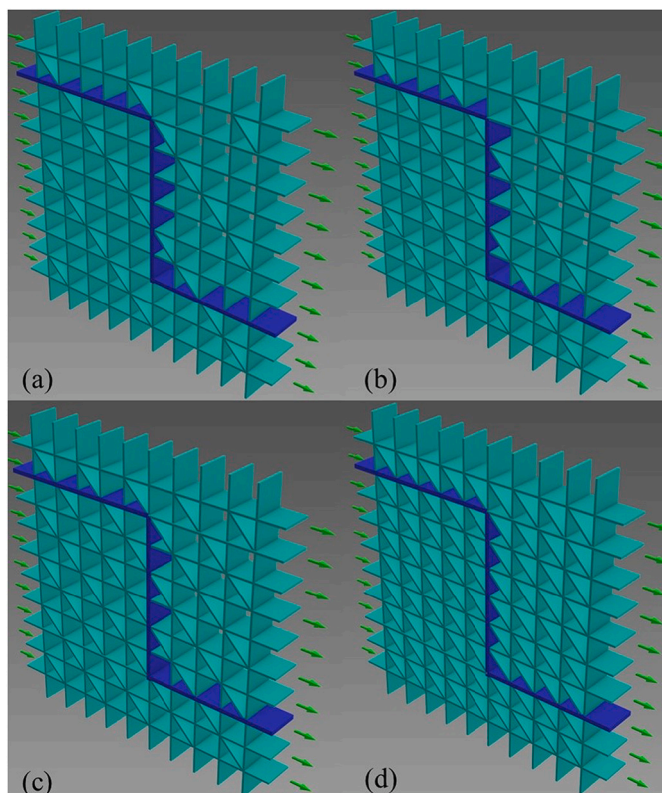


Fig. 8. The configurations of the two-dimensional discrete fracture network with various relative fracture densities of, (a) 0.77, (b) 0.79, (c) 0.85, and (d) 1.0.

density is increased from 0.58 to 0.72 illustrates that adding fractures perpendicular to the hydraulic gradient has no noticeable effect on the total flowrate.

4. Discussion

In this study, a new approach of explicitly considering the groundwater flow characteristic in each fracture is formulated to simulate groundwater flows in three-dimensional discrete fracture networks. The approach uses the laminar flow equation and turbulent flow equation separately for describing laminar and turbulent flows, based on the Reynolds number in each fracture. This approach has the potentials of more accurately quantifying subsurface flow behaviors in real-world scenarios.

For natural fault zones typically composed of a fault core and a cluster of surrounding connected fractures, the fault is the major path of water flow. The flow velocity in the fault could be so high that the relationship between the velocity and the hydraulic gradient is non-linear. For example, estimated flows throughout the complete length of the fault zone under natural circumstances may vary from 170 to 200 m³/day through conduits that do not follow linear flow behaviors (Roques et al., 2014). The region in the aquifer near the fault is most likely affected by the turbulent flow (Shi et al., 2018). It is, therefore, of vital importance to reasonably describe the non-linear flow behavior of groundwater outburst through faults using non-linear equations and to estimate flowrates in fractures located far away from the faults using linear equations.

Pumping well tests are usually carried out on the assumption that flow across fracture networks follows a linear relationship between the velocity and pressure gradient. However, such a linear relation is valid only if the pressure gradient or flow velocity is adequately low (Wen et al., 2006; Pujades et al., 2016). When the *Re* exceeds the critical value, the flow condition becomes non-linear and has a significant impact on well and reservoir performance. Wang et al. (2014) showed that non-linear flow predominates when groundwater flow velocity is

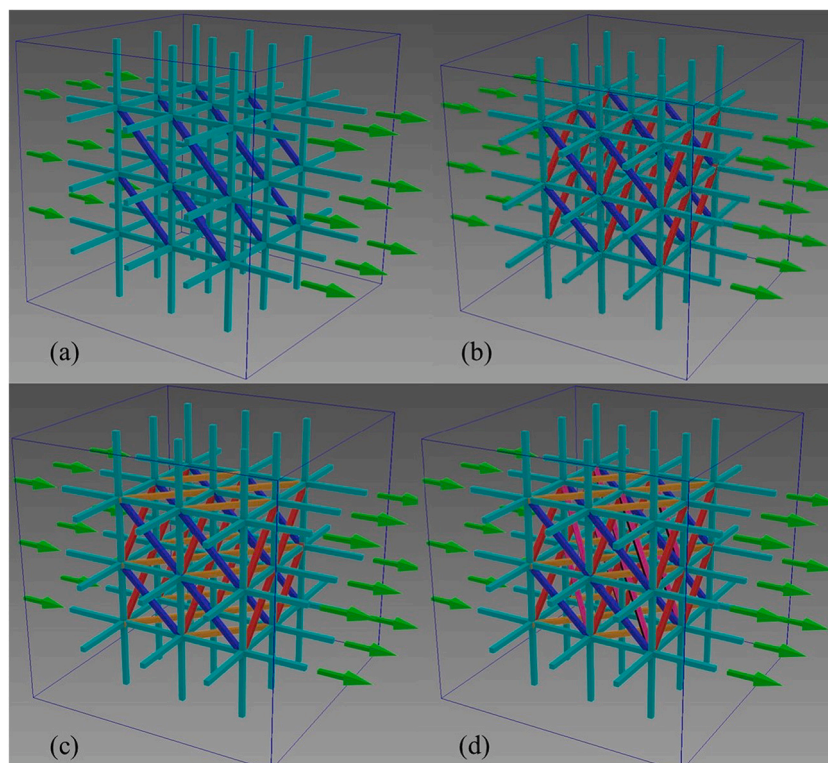


Fig. 9. Portion of the three-dimensional discrete fracture networks with varying relative fracture densities of, (a) 0.58, (b) 0.72, (c) 0.87, and (d) 1.0.

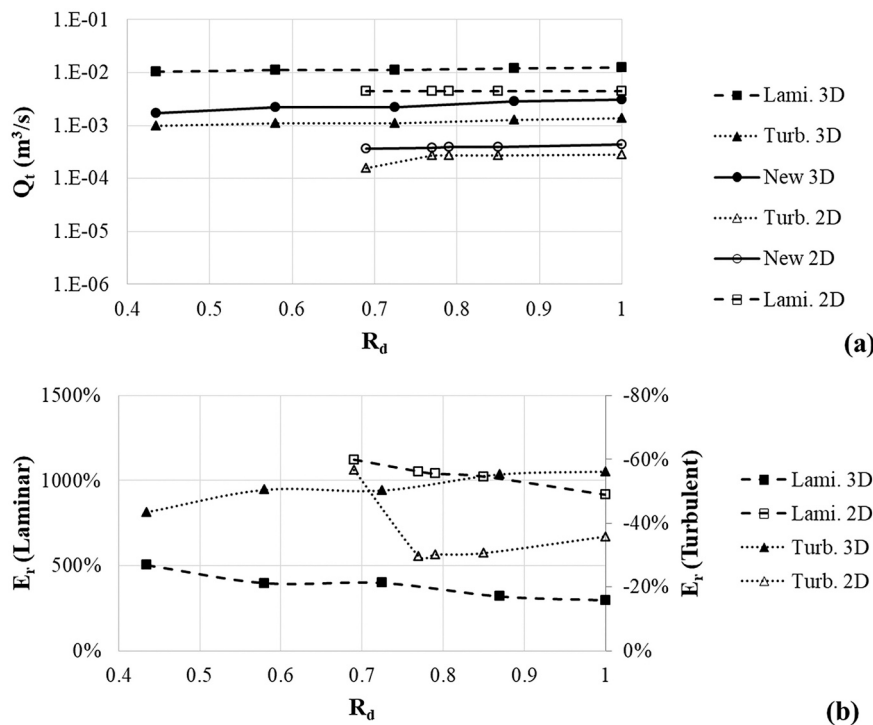


Fig. 10. Flowrate results as a function of the relative fracture density (R_d) of fracture networks shown in Figs. 4, 8 and 9 where the relative density of the two-dimensional and the three-dimensional flow networks varies from 0.69 to 1 and 0.43 to 1, respectively, (a) flowrate, (b) percent flowrate errors.

sufficiently high. Non-linear flow can diminish effective fracture conductivity in the near-well zone (Garipov and Hui, 2019). Other studies also have concluded that the non-linear flows could affect hydraulically fractured wells (Li et al., 2021). Non-linear flow also affects well productivity and total resource recovery in a fractured geothermal reservoir (Legarth et al., 2005; Ni et al., 2011). The study by Zhang and Xing (2012) showed that ignoring non-linear effects while constructing fractures could result in inferior fracture design and type selection.

One of the most important tasks of underground engineering is to predict water intake into a mine tunnel, pumping need and the extent of groundwater management measures. They also reflect the potential severity of other water-related issues, such as difficult and risky tunnel conditions, instability induced by water pressure, lowering of the water table, and draining of surface wells (Botha et al., 2018). As a tunnel approaches the more highly fractured near-surface rock, water inflow rises dramatically. The connection between the inrush velocity and pressure gradient in a fractured rock mass is clearly nonlinear (Huang et al., 2018). As a result, developing a nonlinear flow model to forecast water inrush is of major theoretical and practical importance.

5. Conclusions

In this study, we develop a new model for simulating steady-state groundwater flow behavior in fracture networks by separating laminar flows and turbulent flows in individual fractures. The model compares favorably with field observation data of groundwater flowrates in fractures in a mining site. We then mainly examine the potential errors in groundwater flowrate simulations if the same formulation is used indiscriminately in all fractures and the flowrate differences between the three-dimensional and two-dimensional fracture networks. The influence of various parameters including overall hydraulic gradient, aperture size, total width in the third dimension, and relative density of fractures on the groundwater flowrates is investigated and discussed. The major conclusions can be summarized as follows:

1. Similar to the two-dimensional fracture network counterpart, using the laminar flow equation in all fractures over-predicts

groundwater flowrates while using the turbulent flow equation underestimates them.

2. In general, total groundwater flowrate in the three-dimensional fracture network is larger than that in the two-dimensional network even when the total inlet and outlet fracture areas for these two cases are the same.

3. The contrast of the aperture between large and small fractures significantly affects the potential errors of indiscriminately applying the laminar flow equation or the turbulent flow equation and also influences the flowrate difference between the three-dimensional and two-dimensional fracture networks under otherwise similar conditions.

4. Total groundwater flowrates increase with the density of fractures in both the three-dimensional and two-dimensional fracture networks with most significant increase occurring when more fractures are added in the direction parallel to the overall hydraulic gradient.

Disclosure statement

No potential conflict of interest was reported by the authors.

CRediT authorship contribution statement

Hong Fang: Methodology, Writing – original draft. **Jianting Zhu:** Conceptualization, Data curation. **Jinrong Qiu:** Writing – review & editing. **Yaoming Su:** Data curation. **Di Xia:** Data curation, Visualization.

Declaration of Competing Interest

All authors declare that No conflict of interest exists.

Acknowledgments

This study was supported by: Key-Area Research and Development Program of Guangdong Province (2019B110205002), the Wyoming Center for Environmental Hydrology and Geophysics (WyCEHG) funded

by NSF EPS-1208909 and the National Pilot Project for Prevention and Control of Groundwater Pollution (4401800-202011-140300-0042).

References

- Adler, P.M., Thovert, J.F., 1999. *Fractures and Fracture Networks*, vol. 15. Springer Science & Business Media.
- Agharazi, A., Martin, C.D., Tannant, D.D., 2015. Numerical analysis of plate-load test results on fractured rocks using an equivalent-continuum model: case study of the Bakhtary dam site. *Int. J. Geomech.* 15 (1), 05014001. [https://doi.org/10.1061/\(ASCE\)GM.1943-5622.0000415](https://doi.org/10.1061/(ASCE)GM.1943-5622.0000415).
- Aldrich, G., Hyman, J.D., Karra, S., Gable, C.W., Makedonska, N., Viswanathan, H., Woodring, J., Hamann, B., 2017. Analysis and visualization of discrete fracture networks using a flow topology graph. *IEEE Trans. Visual. Comput. Graphic* 23 (8), 1896–1909. <https://doi.org/10.1109/TVCG.2016.2582174>.
- Botha, S., Roux, J.D., Craig, I.K., 2018. Hybrid non-linear model predictive control of a run-of-mine ore grinding mill circuit. *Miner. Eng.* 123, 49–62. <https://doi.org/10.1016/j.mineng.2018.04.016>.
- Brutz, M., Rajaram, H., 2017. Coarse-scale particle tracking approaches for contaminant transport in fractured rock. *Appl. Math. Model.* 41, 549–561. <https://doi.org/10.1016/j.apm.2016.09.023>.
- Butscher, C., Huguenberger, P., Zechner, E., 2011. Impact of tunneling on regional groundwater flow and implications for swelling of clay–sulfate rocks. *Eng. Geol.* 117 (3–4), 198–206. <https://doi.org/10.1016/j.enggeo.2010.10.018>.
- Carrier, B., Granet, S., 2012. Numerical modeling of hydraulic fracture problem in permeable medium using cohesive zone model. *Eng. Fract. Mech.* 79, 312–328. <https://doi.org/10.1016/j.engfractmech.2011.11.012>.
- Chesnaux, R., Allen, D.M., Jenni, S., 2009. Regional fracture network permeability using outcrop scale measurements. *Eng. Geol.* 108 (3–4), 259–271. <https://doi.org/10.1016/j.enggeo.2009.06.024>.
- Cliffe, K., Holton, D., Houston, P., Jackson, C., Joyce, S., Milne, A., 2011. Conditioning discrete fracture network models of groundwater flow. *Int. J. Numer. Anal. Model.* 8 (4), 543–565.
- Dershowitz, W.S., 1999. Derivation of equivalent pipe network analogues for three-dimensional discrete fracture networks by the boundary element method. *Water Resour. Res.* 35 (9), 2685–2691. <https://doi.org/10.1029/1999WR900118>.
- Dippenaar, M.A., Van Rooy, J.L., 2016. On the cubic law and variably saturated flow through discrete open rough-walled discontinuities. *Int. J. Rock Mech. Min. Sci.* 89, 200–211. <https://doi.org/10.1016/j.ijrmmms.2016.09.011>.
- Follin, S., Stigsson, M., 2014. A transmissivity model for deformation zones in fractured crystalline rock and its possible correlation to in situ stress at the proposed high-level nuclear waste repository site at Forsmark, Sweden. *Hydrogeol. J.* 22 (2), 299–311. <https://doi.org/10.1007/s10040-013-1078-9>.
- Gan, Q., Elsworth, D., 2016. A continuum model for coupled stress and fluid flow in discrete fracture networks. *Geomech. Geophys. Geo-Energy Geo-Resour.* 2 (1), 43–61. <https://doi.org/10.1007/s40948-015-0020-0>.
- Garipov, T.T., Hui, M.H., 2019. Discrete Fracture Modeling approach for simulating coupled thermo-hydro-mechanical effects in fractured reservoirs. *Int. J. Rock Mech. Min. Sci.* 122, 104075. <https://doi.org/10.1016/j.ijrmmms.2019.104075>.
- Gong, J., Rossen, W.R., 2016. Shape factor for dual-permeability fractured reservoir simulation: effect of non-uniform flow in 2D fracture network. *Fuel* 184, 81–88. <https://doi.org/10.1016/j.fuel.2016.06.113>.
- Guo, J., Wang, J., Liu, Y., Chen, Z., Zhu, H., 2017. Analytical analysis of fracture conductivity for sparse distribution of proppant packs. *J. Geophys. Eng.* 14 (3), 599–610. <https://doi.org/10.1088/1742-2140/aa6215>.
- Hadgu, T., Karra, S., Kalinina, E., Makedonska, N., Hyman, J.D., Klise, K., Viswanathan, H.S., Wang, Y., 2017. A comparative study of discrete fracture network and equivalent continuum models for simulating flow and transport in the far field of a hypothetical nuclear waste repository in crystalline host rock. *J. Hydrol.* 553, 59–70. <https://doi.org/10.1016/j.jhydrol.2017.07.046>.
- Huang, N., Jiang, Y., Liu, R., Li, B., 2017. Estimation of permeability of 3-D discrete fracture networks: an alternative possibility based on trace map analysis. *Eng. Geol.* 226, 12–19. <https://doi.org/10.1016/j.enggeo.2017.05.005>.
- Huang, Z., Li, X., Li, S., Zhao, K., Zhang, R., 2018. Investigation of the hydraulic properties of deep fractured rocks around underground excavations using high-pressure injection tests. *Eng. Geol.* 245, 180–191. <https://doi.org/10.1016/j.enggeo.2018.07.020>.
- Huang, N., Jiang, Y., Liu, R., Li, B., Sugimoto, S., 2019. A novel three-dimensional discrete fracture network model for investigating the role of aperture heterogeneity on fluid flow through fractured rock masses. *Int. J. Rock Mech. Min. Sci.* 116, 25–37.
- Huang, L., Su, X., Tang, H., 2020. Optimal selection of estimator for obtaining an accurate three-dimensional rock fracture orientation distribution. *Eng. Geol.* 270, 105575. <https://doi.org/10.1016/j.enggeo.2020.105575>.
- Hyman, J.D., Hagberg, Srinivasan, A.G., Mohd-Yusof, J., Viswanathan, H., 2017. Predictions of first passage times in sparse discrete fracture networks using graph-based reductions. *Phys. Rev. E* 96 (1), 013304. <https://doi.org/10.1103/PhysRevE.96.013304>.
- Ji, S.H., Koh, Y.K., 2017. Appropriate domain size for groundwater flow modeling with a discrete fracture network model. *Groundwater* 55 (1), 51–62. <https://doi.org/10.1111/gwat.12435>.
- Jing, Y., Armstrong, R.T., Mostaghimi, P., 2020. Image-based fracture pipe network modelling for prediction of coal permeability. *Fuel* 270, 117447. <https://doi.org/10.1016/j.fuel.2020.117447>.
- Jourde, H., Cornaton, F., Pistre, S., Bidaux, P., 2002. Flow behavior in a dual fracture network. *J. Hydrol.* 266 (1–2), 99–119. [https://doi.org/10.1016/S0022-1694\(02\)00120-8](https://doi.org/10.1016/S0022-1694(02)00120-8).
- Karimzade, E., Sharifzadeh, M., Zarei, H.R., Shahriar, K., Seifabad, M.C., 2017. Prediction of water inflow into underground excavations in fractured rocks using a 3D discrete fracture network (DFN) model. *Arab. J. Geosci.* 10 (9), 206. <https://doi.org/10.1007/s12517-017-2987-z>.
- Klammler, H., Hatfield, K., Newman, M.A., Cho, J., Annable, M.D., Parker, B.L., Cherry, J.A., Perminova, I., 2016. A new device for characterizing fracture networks and measuring groundwater and contaminant fluxes in fractured rock aquifers. *Water Resour. Res.* 52 (7), 5400–5420. <https://doi.org/10.1002/2015WR018389>.
- Lee, S.D., Moon, H.K., 2004. Hydro-mechanical modelling of tunnel excavation in fractured rock masses by a 3-D discrete fracture network approach. *Int. J. Rock Mech. Mining Sci.* 41 (3), 482. <https://doi.org/10.1016/j.ijrmmms.2004.03.112>.
- Legarth, B., Huenges, E., Zimmermann, G., 2005. Hydraulic fracturing in a sedimentary geothermal reservoir: results and implications. *Int. J. Rock Mech. Min. Sci.* 42 (7–8), 1028–1041. <https://doi.org/10.1016/j.ijrmmms.2005.05.014>.
- Li, W., Zhao, H., Wu, H., Wang, L., Sun, W., Ling, X., 2020. A novel approach of two-dimensional representation of rock fracture network characterization and connectivity analysis. *J. Pet. Sci. Eng.* 184, 106507. <https://doi.org/10.1016/j.petrol.2019.106507>.
- Li, Y., Zhou, Z., Shen, Q., Zhuang, C., Wang, P., 2021. Two-region Darcian and non-Darcian flow towards a well with exponentially decayed rates considering time-dependent critical radius. *J. Hydrol.* 601, 126712. <https://doi.org/10.1016/j.jhydrol.2021.126712>.
- Mathurin, F.A., Astrom, M.E., Laaksoharju, M., Kalinowski, B.E., Tullborg, E.L., 2012. Effect of tunnel excavation on source and mixing of groundwater in a coastal granitoid fracture network. *Environ. Sci. Technol.* 46 (23), 12779–12786. <https://doi.org/10.1021/es301722b>.
- Mattila, J., Tammisto, E., 2012. Stress-controlled fluid flow in fractures at the site of a potential nuclear waste repository, Finland. *Geology* 40 (4), 299–302. <https://doi.org/10.1130/G32832.1>.
- Montecinos, C., Wallace, K., 2010. Equivalent roughness for pressure drop calculations in mine ventilation. In: *Proceedings of the 13th US/North American Mine Ventilation Symposium*, pp. 225–230.
- Ni, J.C., Cheng, W., Ge, L., 2011. A case history of field pumping tests in a deep gravel formation in the Taipei Basin, Taiwan. *Eng. Geol.* 117 (1–2), 17–28. <https://doi.org/10.1016/j.enggeo.2010.10.001>.
- Oliver, J., Caicedo, M., Roubin, E., Huespe, A.E., Hernandez, J.A., 2015. Continuum approach to computational multiscale modeling of propagating fracture. *Comput. Method Appl. Mech. Eng.* 294, 384–427. <https://doi.org/10.1016/j.cma.2015.05.012>.
- Pan, J., Lee, C., Lee, C., Yeh, H., Lin, H., 2010. Application of fracture network model with crack permeability tensor on flow and transport in fractured rock. *Eng. Geol.* 166 (1–2), 166–177. <https://doi.org/10.1016/j.enggeo.2010.08.007>.
- Parashar, R., Reeves, D.M., 2012. On iterative techniques for computing flow in large two-dimensional discrete fracture networks. *J. Comput. Appl. Math.* 236 (18), 4712–4724. <https://doi.org/10.1016/j.cam.2012.02.038>.
- Pujades, E., Jurado, A., Carrera, J., Vazquez-Sune, E., Dassargues, A., 2016. Hydrogeological assessment of non-linear underground enclosures. *Eng. Geol.* 207, 91–102. <https://doi.org/10.1016/j.enggeo.2016.04.012>.
- Reeves, D.M., Parashar, R., Pohll, G., Carroll, R., Badger, T., Willoughby, K., 2013. The use of discrete fracture network simulations in the design of horizontal hillslope drainage networks in fractured rock. *Eng. Geol.* 163, 132–143. <https://doi.org/10.1016/j.enggeo.2013.05.013>.
- Ren, F., Ma, G., Fu, G., Zhang, K., 2015. Investigation of the permeability anisotropy of 2D fractured rock masses. *Eng. Geol.* 196, 171–182. <https://doi.org/10.1016/j.enggeo.2015.07.021>.
- Roques, C., Bour, O., Aquilina, L., Dewandel, B., Leray, S., Schroetter, J.M., et al., 2014. Hydrological behavior of a deep sub-vertical fault in crystalline basement and relationships with surrounding reservoirs. *J. Hydrol.* 509, 42–54. <https://doi.org/10.1016/j.jhydrol.2013.11.023>.
- Sarpkaya, T., 1966. Experimental determination of the critical Reynolds number for pulsating Poiseuille flow. *J. Basic Eng.* 88 (3), 589–598. <https://doi.org/10.1115/1.3645920>.
- Shi, W., Yang, T., Liu, H., Yang, B., 2018. Numerical modeling of non-Darcy flow behavior of groundwater outburst through fault using the Forchheimer equation. *J. Hydrol. Eng.* 23 (2). [https://doi.org/10.1061/\(ASCE\)HE.1943-5584.0001617](https://doi.org/10.1061/(ASCE)HE.1943-5584.0001617).
- Sutera, S.P., Skalak, R., 1993. The history of Poiseuille's law. *Annu. Rev. Fluid Mech.* 25 (1), 1–20.
- Swamee, P.K., Jain, A.K., 1976. Explicit equations for pipe flow problems. *J. Hydraul. Div.* 102 (5), 657–664.
- Tang, C.A., Yang, W.T., Fu, Y.F., Xu, X.H., 1998. A new approach to numerical method of modelling geological processes and rock engineering problems — continuum to discontinuum and linearity to nonlinearity. *Eng. Geol.* 49 (3–4), 207–214. [https://doi.org/10.1016/S0013-7952\(97\)00051-3](https://doi.org/10.1016/S0013-7952(97)00051-3).
- Wang, Q., Zhan, H., Tang, Z., 2014. Forchheimer flow to a well-considering time-dependent critical radius. *Hydrol. Earth Syst. Sci.* 18 (6), 2437–2448. <https://doi.org/10.5194/hess-18-2437-2014>.
- Wen, Z., Huang, G., Zhan, H., 2006. Non-Darcian flow in a single confined vertical fracture toward a well. *J. Hydrol.* 330 (3–4), 698–708. <https://doi.org/10.1016/j.jhydrol.2006.05.001>.
- Wu, R., Kresse, O., Weng, X., Cohen, C.-E., Gu, H., 2012. Modeling of interaction of hydraulic fractures in complex fracture networks. In: *Paper Presented at SPE*

- Hydraulic Fracturing Technology Conference, Society of Petroleum Engineers. <https://doi.org/10.2118/152052-MS>.
- Xu, Z., Hu, B.X., 2017. Development of a discrete-continuum VDFST-CFP numerical model for simulating seawater intrusion to a coastal karst aquifer with a conduit system. *Water Resour. Res.* 53 (1), 688–711. <https://doi.org/10.1002/2016WR018758>.
- Zhang, J., Xing, H., 2012. Numerical modeling of non-Darcy flow in near-well region of a geothermal reservoir. *Geothermics* 42, 78–86. <https://doi.org/10.1016/j.geothermics.2011.11.002>.